Journal of Materials Chemistry A

ROYAL SOCIETY OF CHEMISTRY

PAPER

View Article Online
View Journal | View Issue

Cite this: J. Mater. Chem. A, 2024, 12, 28899

Carbonate deprotonation on an Ni-rich layered cathode: development of a new *cis*-oligomer as an organic coverage†

Laurien Merinda,[a] Fu-Ming Wang, *[abcd] Nae-Lih Wu, *[eg] Rio Akbar Yuwono,[a] Chusnul Khotimah,[a] Ulya Qonita,[a] Wei-Hsiang Huang,[f] Lester Pei-Wan Tiong,[a] Ching-Kai Chang,[a] Ping-Hsuan Hsu,[a] Chih-Wen Pao,[f] Jeng-Lung Chen, [f] Chi-Liang Chen [f] and Ting-Shang Chan[f]

Ni-rich layered cathodes have a high practical capacity (>200 mA h g^{-1}) and tapped density (>3.6 mg cm^{-2}) and have thus attracted widespread attention in significant applications such as electric vehicles and energy storage. However, the high surface reactivity of these cathodes promotes the decomposition of carbonate solvents, which contributes to the growth of the cathode–electrolyte interphase (CEI) as well as rapid fading of the battery's capacity during long-term cycling. Carbonates are favorable for the deprotonation reaction by the oxygen atom in the Ni-rich layered cathode and in the formation of the CEI. In this study, the deprotonation mechanism of cyclic and linear carbonates on a Ni-rich layered cathode was thoroughly investigated using *operando* Fourier-transfer infrared spectroscopy, and the reasons for cathode fading could be confirmed in terms of carbonate structures. In addition, a new maleimide oligomer was developed and coated on a Ni-rich layered cathode to inhibit the deprotonation of the carbonates. The maleimide oligomer acts as a *cis* isomer that provides a bridge function for reacting with oxygen on the cathode surface through its cis configuration. Moreover, this bridge function will keep the carbonates away from the cathode surface for further decomposition during cycling. On the contrary, battery performance exhibited a cycling ability at a high rate, and the new cis–maleimide oligomer helped improve rate capability. A full-cell (>3 A h) containing graphite as the anode coated with the maleimide oligomer in its cis form was fabricated.

Received 26th July 2024
Accepted 24th September 2024

DOI: 10.1039/d4ta05197a

rsc.li/materials-a

Introduction

Lithium-ion batteries (LIBs) have been the most promising energy storage device since 1991. Currently, the demand for EVs is expected to increase to 2200 GW h of the global storage capacity by 2030.[1,2] In this regard, layered Ni-rich oxide cathodes are a promising candidate to fulfill this demand because of their high capacity. Currently, the energy density of LIBs has increased to a range of 250–300 W h kg^{-1} owing to the adoption of layered Ni-rich oxide cathodes such as $LiNi_{0.8}Co_{0.1}Mn_{0.1}O_2$ (NCM811) and $LiNi_{0.85}Co_{0.1}Al_{0.05}O_2$ (NCA). However, layered Ni-rich oxide cathodes face some issues that can lead to capacity fading and thermal instability.[3–5]

The mechanical failure and surface reconstruction of layered Ni-rich oxide cathodes are the main factors responsible for these shortcomings.[5,6] Typically, mechanical failure is correlated with bulk structural stability, which depends on the amount of nickel content and cut-off potential.[5,7] Meanwhile, surface reconstruction is known to occur at a relatively low potential of 3.8 V.[8–10] Therefore, the layered Ni-rich oxide cathode material is most likely to suffer from surface reconstruction during the cycling process. Moreover, the battery management system (BMS) for EV application introduces "grace capacity", in which battery capacity is designed to exceed the minimum requirement. This limits the state of charge (SOC) and depth of discharge (DOD) to 80%. In the case of NCM811, this capacity utilization guarantees its structural stability.[11,12] Recently, a previous study observed at the cell level that NCM811 maintained a layered structure ordering after 500

[a]Graduate Institute of Applied Science and Technology, National Taiwan University of Science and Technology, Taipei 10607, Taiwan. E-mail: mccabe@mail.ntust.edu.tw
[b]Graduate Institute of Energy and Sustainability Technology, National Taiwan University of Science and Technology, Taipei 10607, Taiwan
[c]Department of Chemical Engineering, Chung Yuan Christian University, Taoyuan 320314, Taiwan
[d]R&D Center for Membrane Technology, Chung Yuan Christian University, Taoyuan 320314, Taiwan
[e]Department of Chemical Engineering, National Taiwan University, Taipei 10617, Taiwan. E-mail: nlw001@ntu.edu.tw
[f]National Synchrotron Radiation Research Center, Hsinchu 30076, Taiwan
[g]Advanced Research Center for Green Materials Science and Technology, National Taiwan University, Taipei 10617, Taiwan

† Electronic supplementary information (ESI) available. See DOI: https://doi.org/10.1039/d4ta05197a

cycles.[13] However, the cathode only retained 15.6% of its initial capacity after 500 cycles. It was found that the poor cycling stability of NCM811 was due to an interfacial issue, which correlated with the surface structure.

Surface reconstruction occurs when the delithiated Ni-rich cathode interacts with the electrolyte, owing to the presence of Ni^{4+} and reactive oxygen species.[4,10,14] Ni^{4+} is unstable because it has a partially filled 3d shell. The additional repulsion between the electrons in the partially filled shell is easily influenced by the surrounding environment. Therefore, Ni^{4+} is reduced to a low-valence state, mainly Ni^{2+}, along with oxygen evolution. This leads to the electrolyte decomposition,[8,10] release of gaseous products,[14] and formation of an undesirable cathode–electrolyte interphase (CEI).[15,16] Hence, the interaction between the surface of the layered Ni-rich oxide cathode and electrolyte plays an important role for the cycling performance.

The decomposition of the electrolyte occurs *via* chemical and electrochemical oxidation processes.[17] In the case of Ni-rich cathodes, Gasteiger *et al.* reported that the alkyl electrolyte decomposition occurs *via* chemical oxidation.[17] Therefore, this type of electrolyte decomposition is strongly related to the cathode surface reactivity in the charged condition. In NCM811, the surface reactivity is associated with the presence of the active oxygen from the Ni–O bond covalency (increases with increasing Ni content). Thus, it promotes high nucleophilicity of the surface-active oxygen, which thermodynamically triggers the dehydrogenation of carbonate solvents on the NCM811 surface.[18]

Zhang *et al.* constructed an *in situ* FTIR method and density functional theory (DFT) approach to investigate and confirm the dehydrogenation pathways of ethylene carbonate (EC) on the NCM811 surface.[8] The study revealed that the EC dehydrogenation generated some species; such as dehydrogenated EC (de-H EC), in which one hydrogen is removed from the structure; vinylene carbonate (VC) by the removal of two hydrogens; and oligomerization of EC (ring-opening EC). Furthermore, the de-H EC species anchor onto the oxide surface, while the VC and oligomerization EC species diffuse into the electrolyte. Furthermore, Grey *et al.* found that charged NCM811 at high SOC (>80%) releases reactive $^1O_2$, which chemically oxidized VC to form gaseous products, such as CO_2, CO, and H_2O.[10] The presence of an active oxygen singlet from NCM811 easily attacks the cyclic and linear carbonate solvents, which lead to electrolyte decomposition, thus releasing gaseous products and an undesirable CEI film.[14]

Several review articles have introduced studies on protective coatings, such as coating the cathode with PEDOT,[19] amorphous Nb_2O_5,[20] restructuring the electrode through *in situ* and *ex situ* templating of the pore structure,[21] and a hyperbranched oligomer.[22–24] To inhibit the decomposition of EC on Ni-rich cathodes, Yu *et al.* substituted the oxygen with fluorine on the surface to decrease the energetic driving force for EC deprotonation.[25]

In this work, the reactions of carbonate solvents on a Ni-rich cathode were investigated by *operando* FTIR, chemical composition analysis, and electrochemical measurements. Based on *operando* FTIR results, this work presents a clear deprotonation reaction and the reaction sequence on carbonate solvents. Furthermore, to prevent the deprotonation reaction on the Ni-rich cathode, an oligomer was developed by a cis isomerism (CI) design. This new oligomer provides a bridge function between the surface oxygen and the electrolyte by its cis structure formulation. Finally, a pouch cell (3 A h) designed with NMC811/graphite was used for testing performance, including a hybrid pulse power characterization (HPPC) test.

Experimental methods

Materials

Polycrystalline $LiNi_{0.8}Co_{0.1}Mn_{0.1}O_2$ (NCM811, UBIQ Technology Co., Ltd, Taiwan), Super-P (UBIQ Technology Co., Ltd), and polyvinylidene difluoride (PVDF HSV 1800, Kynar) were used as the cathode active material, carbon black, and binder, respectively. Polyethylene (PE) microporous film (7 μm, Asahi Kasei's, HIPORE™) was used as the separator. As for the electrolyte, 1 M of $LiPF_6$ dissolved in ethylene carbonate (EC) and ethyl methyl carbonate (EMC) (volume ratio of 3 : 7) was utilized and known as LP57. The LP57 electrolyte was purchased from Shenzhen Capchem Technology Co., Ltd. *n*-Methyl-2-pyrrolidone (NMP, UBIQ Technology Co., Ltd) was utilized as the solvent for the electrode preparation and the cis isomerism (CI) oligomer. *n*,*n*-(1,4-Phenylene)di-maleimide (Tokyo Chemical Industry Co., Ltd) was used as the precursor to synthesize the CI oligomer.

Synthesis of the cis isomerism (CI) oligomer

The CI oligomer was synthesized by dissolving *n*,*n*-(1,4-phenylene)di-maleimide in NMP *via* continuous stirring in a heated oil bath at 150 °C for 3 h. The optimal concentration for dissolution was 1 wt% of *n*,*n*-(1,4-phenylene)di-maleimide in NMP solution. This solution was then stored in a refrigerator (4 °C) to prevent thermal degradation. The CI-covered NCM811 (CI@NCM811) was prepared by CI oligomer solution with NCM811 during the slurry preparation. The presence of the CI oligomer on NCM811 was confirmed with a change in the surface morphology of the fresh electrode (Fig. S1†), and a change in the intensity of the transition metal vibrational mode (Fig. S2†).

Electrode and free-standing electrode preparations

Pristine NCM811/CI@NCM811, 5 wt% PVDF in NMP (binder solution), and super-P were vigorously mixed (1400 rpm) at a solid ratio of 8 : 1 : 1 until a homogenous slurry was formed. Then, the slurry was casted onto an Al current collector using a 150 μm doctor blade. After coating, the electrode was dried in an oven at 100 °C for 1 h. The dried electrode was calendered using a rolling machine to increase the electrode density, and then punched into 12 mm-diameter circular disks for a half-cell test. The prepared electrode was vacuum-dried at 100 °C overnight to completely remove any excess NMP. The graphite anode comprised 93 wt% meso-carbon-micro-beads (MCMB-2528, Osaka Gas), 3 wt% KS6 as a conductive additive, and 4 wt% PVDF as a binder. The anode-to-cathode (A/C) ratio of the full cell was designed to be 1.05.

The free-standing electrodes for the *in-operando* ATR FTIR test were prepared by mixed NCM811/CI@NCM811, PVDF in NMP (binder solution), and Super-P at ratio of 8 : 1 : 1. These materials then stirred in 1400 rpm for 1 h and cast onto a glass fiber membrane (Whatman GF/D Separator Membrane, 110 mm in diameter). The cast electrodes were dried in a 70 °C oven for 1 h. The free-standing electrode was calendered and punched into 12 mm-diameter circular disks. The final electrodes with ~9.2 mg cm^{-2} of active material loading were dried at 100 °C under overnight vacuum.

Electrochemical measurements

The half-cell configurations were assembled into a CR2032-type coin cell in an Ar-filled glovebox, along with a lithium metal foil as the counter electrode. Cyclic voltammetry (CV) tests were performed using a VMP3 potentiostat (BioLogic) at a scanning rate of 0.1 mV s^{-1} in a potential range of 2.8–4.6 V (*vs.* Li/Li^+). The galvanostatic charge–discharge process of the half-cell configurations was evaluated using a Neware battery test (BTS4000). Prior to the cycle test, two formation cycle tests were performed at a potential range of 2.8–4.3 V (*vs.* Li/Li^+) at 25 °C in a current rate of 0.1C. Then, the long cycle performance was conducted at 1C under a similar potential range and temperature condition. The formation and long cycle tests were both conducted in a constant-current–constant-voltage (CCCV) mode and a constant-current (CC) mode for charging and discharging, respectively. The rate capabilities of the half-cell were evaluated by varying the current rate from 0.1C to 10C in a CCCV charge mode and a CC discharge mode. Electrochemical impedance spectroscopy (EIS) was performed using a VMP3 potentiostat at frequencies ranging from 1 MHz to 10 mHz, and at an amplitude of 10 mV.

Material characterizations

Scanning electron microscopy (SEM, JEOL JSM-6500F) was applied to examine the surface morphology of the electrodes. Fourier transform infrared spectroscopy with attenuated total reflection (FTIR-ATR) was performed using the JASCO 6700 series to collect the IR spectra in the absorption energy range of 400–4000 cm^{-1}. FTIR-ATR was performed in a N_2-filled glovebox to prevent interference from ambient atmosphere. The molecular weight of the oligomer was measured using gel permeation chromatography (SISC-LAB GPC).

In operando experiments

In operando FTIR was conducted using a Jasco Electrochemical cell (Ecc-450+ ATR Pro 450), where germanium was used as its optical prism attached to the prism holder plated with gold. The *operando* cell comprised a free-standing electrode of NMC811 as the positive electrode, lithium metal wrapped in a stainless-steel spacer as the negative electrode, and the separator was assembled in a nitrogen-filled gas glovebox. The cell was equipped with a micrometer head to reduce the cell resistance by adjusting the distance between the electrode and the optical prism surface. The *operando* cell was rested for 3 h before testing. In the *operando* FTIR spectroscopy system, a liquid nitrogen-cooled mercury cadmium telluride detector was used to produce a strong IR absorption and high sensitivity in the range of 5200–650 cm^{-1} with an average of 100 scans for each spectrum. *In situ* X-ray absorption near-edge spectroscopy (XANES) and extended X-ray absorption fine structure (EXAFS) measurements were performed in transmission mode at the TLS 01C1/17C and TPS 44A beamlines of the National Synchrotron Radiation Research Center (NSRRC). Energy calibration was performed using the spectrum of the Ni^0 foil as a reference (Ni K-edge: 8333 eV).

Hybrid pulse power characterization (HPPC) test

HPPC testing: 10% DOD steps were used based on the battery capacity determined from the static capacity test. The steps proceeded from 10% to 80% DOD, and could continue back to 30% DOD for the second half of the test profile. Each step comprised: (1) rest for 60 min, (2) pulse-discharge: 1C for 10 s, (3) rest for 10 min (relaxation period), (4) pulse-regeneration: 1C or 0.75C for 10 s, (5) Rest for 10 min (relaxation period), (6) discharge/charge to next step at the prescribed discharge/charge current rate.

Results and discussion

Deprotonation of EC during charging

To investigate the SOC effects on the electrolyte interaction to NCM811, an *operando* FTIR measurement was performed. Three wavenumber ranges are highlighted in Fig. 1, indicating the variations in the specific functional groups during lithiation and delithiation. As shown in Fig. 1a, the presence of EC and solvated EC-Li^+ can be clearly observed at 1803 cm^{-1} and 1773 cm^{-1}, respectively, at the open circuit voltage (OCV), representing the stretching of C═O and C═O–Li.

Starting from the delithiation, two absorption peaks were gradually formed at 1830 and 1844 cm^{-1}, which can be assigned to the dehydrogenated EC (de-H EC) and vinylene carbonate (VC), respectively.[8] Giordano *et al.* demonstrated that the dissociation of EC based on DFT analysis is energetically favorable on a Ni-rich cathode, and that the reactivity of the dissociation process increases in the high-SOC range.[26] Initially, the de-H EC molecule formed by the first deprotonation step from the EC structure.[8] Then, the EC structure undergoes a second deprotonation and the VC formation proceeds.[8,10] In Fig. 1a, both de-H EC and VC are present at 3.8 V, and the intensity of VC is greater than that of de-H EC. Upon charging to higher SOC, the increasing intensity of de-H EC was followed by an increase of the VC formation. This result indicates that the energy of the second EC deprotonation was weak and almost immediately accompanied the first deprotonation reaction, indicating that the reaction kinetics of EC deprotonation was fast.

Two IR bands are present at 1576 and 1347 cm^{-1} (Fig. 1b and c), which can be assigned to the O–C═O bending vibrations and the C–O–C asymmetric stretching vibration, respectively.[27–30] These O–C═O and C–O–C vibrational modes can be attributed to the carbonate solvent decomposition, which involve the ring opening of EC and possibly bond

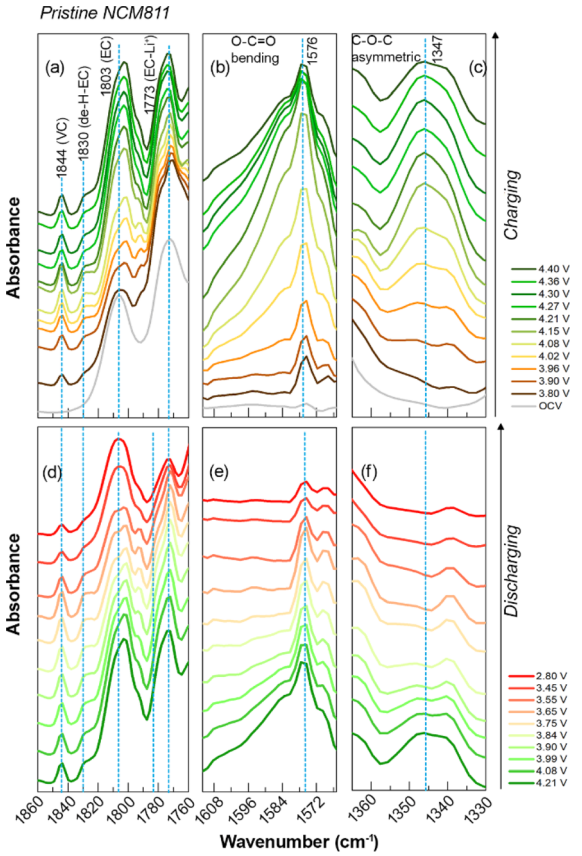

Fig. 1 *Operando* FTIR spectra of pristine NMC811 during (a–c) charging and (d–f) discharging. VC is present at 1844 cm^{-1}, de-H EC at 1830 cm^{-1}, and O–C=O bending vibration at 1573 cm^{-1}. The C–O–C asymmetric stretching vibration is present at 1347 cm^{-1}.

breaking of EMC, respectively. In the OCV state (light grey line), both absorption peaks corresponding to O–C=O and C–O–C were nearly unobservable. However, the intensity of both absorption peaks drastically increased with increasing SOC, indicating that the decomposition of carbonates depends on the electrochemical operation. This phenomenon can be reasonably explained as the carbonates were attracted by the cathode surface oxygen atom for the first deprotonation reactions, which induced the ring opening of EC.[8] Previous studies have demonstrated that carbonates are chemically oxidized as the SOC increases, which is induced by the reactive oxygen species.[10,31]

Deprotonation of EC during discharging

Fig. 1d shows the lithiation reaction of NCM811 from 4.2 to 2.8 V. This figure shows that VC and de-H EC remain on the surface without any significant change. However, less absorbance intensity of VC and de-H EC was detected on the NCM811 surface as the voltage reached the end of discharge. This result is consistent with the study by Rinkel *et al.*, where some the deprotonated EC byproducts are likely diffused away to the anode part for further SEI formation.[10]

In Fig. 1e and f, the intensity of the decomposed EC (1576 cm^{-1}) and EMC (1347 cm^{-1}) rapidly decreased as the SOC decreased. Interestingly, only the decomposed EMC is completely removed from the surface (Fig. 1f). Two new findings can be made from these observations. First, the fragments of the decomposed EC and EMC are not tightly packed on the cathode. Instead, they easily move away from the cathode surface, following the diffusion of the lithium ions during the lithiation, especially the decomposed EMC. Rinkel *et al.* proposed that some of this carbonate's decomposition byproducts diffused to the electrolyte, and possibly further decomposed as a SEI on the negative electrode side.[32]

Second, a part of the decomposed EC remains on the cathode surface after lithiation. This is due to the decomposed EC (ring opening of EC) being energetically favorable to be adsorbed in the delithiated (010) surface facet of the layered structure.[33] This finding further confirms that EC strongly reacts with NCM811 and deposits its decomposed products on the surface, implying a large impedance in a prolonged cycle.

CI layer coverage to reduce the deprotonation of EC

The CI oligomer was fabricated using a maleimide monomer. Fig. S4† shows its proposed structure. The unsaturated C=C bond is expected to react with another one upon free-radical reaction, and further polymerize to a linear structure. As listed in Table S1,† the CI oligomer has a higher polymer dispersity index (PDI) and degree of polymerization (Dp) than the monomer. Previous studies have discussed a compound with a high PDI and Dp, which indicate a wide range distribution of the molecular weight and higher repeat units.[34] Based on the results, the CI is expected to have three to four maleimides for an oligomer formation. This linear oligomer provides coverage on NCM811. Fig. S5a† shows that the monomer exhibits strong C=C bond absorption at 1697 cm^{-1}, which red shifts to 1670 cm^{-1} after CI formation.[35] In addition, as shown in Fig. S5b,† the C=CH bond presents at 3100 cm^{-1} for the monomer and the –COH/–OH bond appears at 1066/3675 cm^{-1} for the CI, indicating that the CI is synthesized from C=C and produces a specific –OH functional group on the structure. Thus, the –OH and C=O groups may arrange to a CI structure, which is hypothesized to provide the bridge function.

To mitigate the decomposed products on the surface, as well as reduce the deprotonation of the carbonate solvents, the CI-covered NCM811 was studied in terms of its bridge function. Fig. 2a shows that the appearance of de-H EC (1830 cm^{-1}) is delayed to 3.9 V. Fig. 2b and c illustrates that the changes in the two IR bands at 1576 and 1347 cm^{-1} are also delayed to 3.9 V. Based on this hypothesis of a bridge function provided by CI coverage, the deprotonation of the EC is evidently weaker due to the isomerism effect on the CI. This is further discussed in Fig. 3a–d, which summarizes the changes in the four specific IR bands with respect to the interaction of EC with NCM811. In Fig. 3a, the formation of VC increases during the delithiation of pristine NCM811 from lower to higher SOC. This transformation of EC to VC was fast, indicating a low reaction barrier on the Ni-rich cathodes. In addition, decomposed EC and EMC fragments (carboxylates group) were rapidly formed upon charging to higher SOC (Fig. 3c and d). On the contrary,

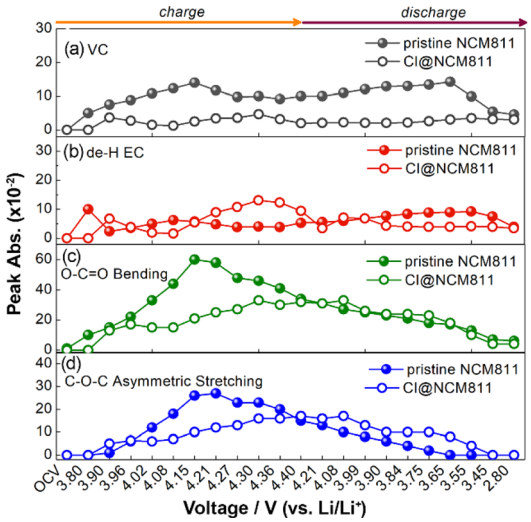

Fig. 2 *Operando* FTIR peak assignment behaviour of pristine NCM811 and CI@NCM811 in the first cycle represented by (a) VC, (b) de-H EC, (c) O–C=O bending vibration and (d) C–O–C asymmetric stretching vibration.

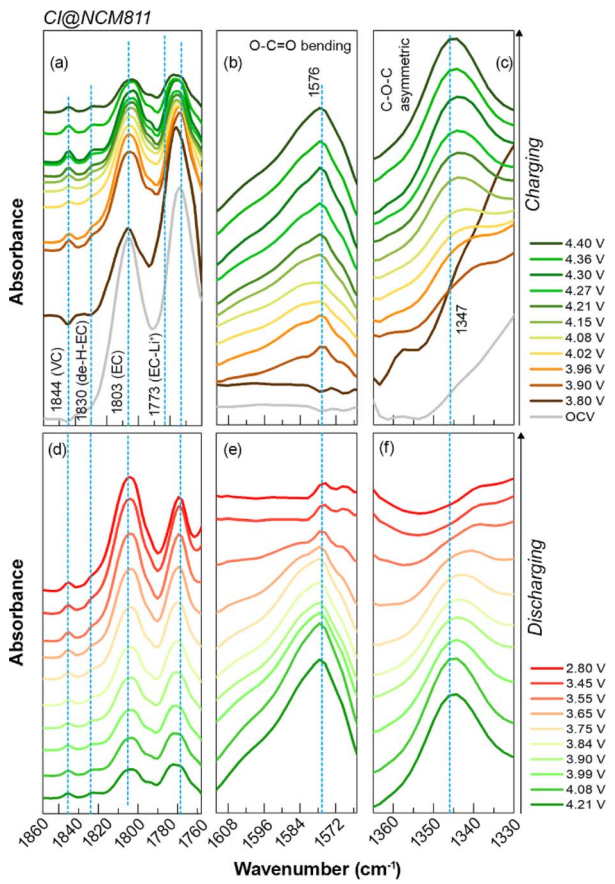

Fig. 3 *Operando* FTIR spectra of CI@NCM811 during (a–c) charging and (d–f) discharging. The VC presents at 1844 cm^{-1}, de-H EC presents at 1830 cm^{-1}, and O–C=O bending vibration presents at 1573 cm^{-1}. The C–O–C asymmetric stretching vibration presents at 1347 cm^{-1}.

CI@NCM811 significantly reduced the formation of VC, as well as the decomposition of the carbonate solvent.

The reactivity of EMC to the NCM811 surface

Although EC formation is the main issue in Ni-rich layered cathodes, several works have suggested that linear carbonates may produce a different CEI, which affects the battery performance.[8,36] Dose *et al.* demonstrated that the methyl group in EMC is active with respect to the reactive O_2 owing to the unbalanced electron cloud (*e.g.*, $^1O_2$), which induces a substitution at the proton position, ultimately forming ethanol and/or gas evolution.[37] In fact, Zhang *et al.* also stated that the EMC would undergo deprotonation (de-H EMC) at high SOC with NCM811, and the protonation occurs at the *b* site position of the EMC structure, as observed by a peak shifting on the FTIR measurement.[8] Yang and coworkers reported on the three different deprotonation EMC products through a density functional theory (DFT) analysis: de-H_a EMC (1761 cm^{-1}), de-H_b EMC (1751 cm^{-1}), and de-H_c EMC (1741 cm^{-1}).[8,38] Fig. 4 shows the *operando* observation of EMC on NCM811. In Fig. 4a, only one main IR absorption band can be found: EMC (1747 cm^{-1}) at OCV. After triggering the voltage by *operando* measurement, the other IR absorption peaks can be immediately observed at 3.8 V: solvated EMC (1717 cm^{-1}), de-H_c EMC (1741 cm^{-1}), de-H_b EMC (1751 cm^{-1}), and de-H_a EMC (1761 cm^{-1}). Among the three deprotonations of EMC, the intensity of de-H_b EMC dominates at high SOC (>3.8 V), which consistent with Zhang's results.[8] However, this *operando* FTIR analysis was the first to detect the presence of de-H_c EMC and de-H_a EMC. Although a few papers have discussed the reaction mechanism of the deprotonation of EMC, it is believed that an asymmetric structure of the EMC causes a nonuniform electron cloud density, and the ethyl group is thereby highly electron-donating for attraction by oxygen on the cathode surface. The domination of de-H_b EMC at high SOC indicates the reactivity of EMC to the delithiated NCM811 surface.

Upon the lithiation of NCM811, Fig. 4b shows that the de-H_b EMC is shifted back to the original wavenumber (original EMC/1747 cm^{-1}) at low SOC. Meanwhile, the other two products (de-H_a and de-H_c EMC) almost completely disappeared at discharge potential of 3.45 V. This result is interesting, in which EMC deprotonation is almost reversible. Regardless of the proton position of the EMC structure, these protons can be recovered back to their original state. This result suggests that the EMC may join the CEI reaction, though at a lower amount.

CI layer coverage to reduce the deprotonation of EMC

In comparison with the bare NCM811, the EMC interaction on the CI@NCM811 was studied. Fig. 4c shows only one main peak (EMC) at 1747 cm^{-1} upon OCV. After starting the *operando* measurement, de-H_a EMC (1761 cm^{-1}), de-H_b EMC (1751 cm^{-1}), and de-H_c EMC (1741 cm^{-1}) can be found at 3.9 V, which is delayed compared to the case of pristine NCM811 (Fig. 4a). Moreover, the intensity of de-H_b EMC was significantly weakened, followed by the weak intensity of de-H_a and de-H_c EMC. By decreasing the SOC in Fig. 4d, the IR bands of the

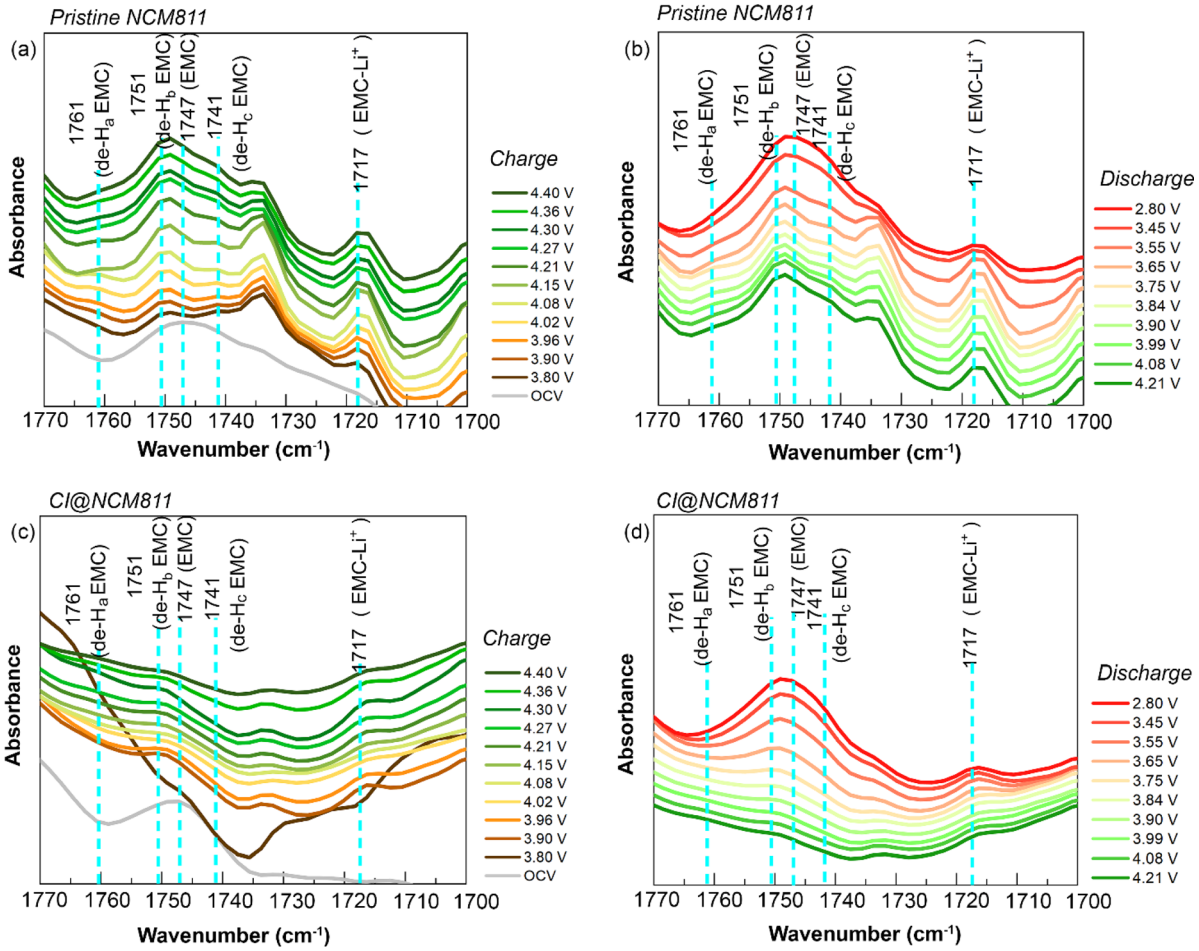

Fig. 4 *Operando* FTIR spectra of pristine NCM811 during (a) charging and (b) discharging as well as of CI@NCM811 during (c) charging and (d) discharging.

aforementioned species return or disappear to their original state like the bare one in Fig. 4b. The result is typically the same as that obtained for pristine NCM811. However, CI@NCM811 seems to repulse the EMC from deprotonation. Fig. 5 shows that the deprotonation is almost eliminated. Previous analysis showed that the CI was constructed by a cis structure, with a –OH group and the C=O group of the CI designed as bridge function between the electrolyte and electrode. There is a potential movement from solvated Li^+ to approach the C=O group of CI during the electrochemical reaction, as discussed in the following subsection.

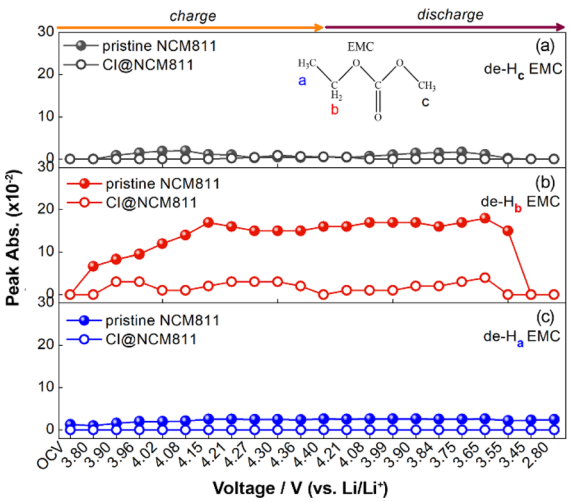

Fig. 5 Peak assignment behavior of pristine NCM811 and CI@NCM811 represented by the absorption intensity of (a) de-H_c EMC at 1741 cm^{-1}, (b) de-H_b EMC at 1751 cm^{-1}, and (c) de-H_a EMC at 1761 cm^{-1}.

Li^+ solvation during charging and discharging

It is known that EMC and EC provide different Li^+ solvation abilities, owing to their dielectric constants. Fig. 6 shows a ratio comparison between the EMC (1747 cm^{-1})/EMC-Li^+ (1717 cm^{-1}) and EC (1806 cm^{-1})/EC-Li^+ (1773 cm^{-1}) in the first electrochemical reaction. A ratio greater than 1 indicates that the desolvation is dominant; a ratio less than 1 indicates that solvation is dominant. Fig. 6a indicates that EC and EMC are not favorable to solvate Li^+ at the OCV state. After charging, Li^+ delithiated from the bulk cathode and diffused to the electrolyte. In this result, Li^+ shows a solvation behavior (ratio < 1) with EC and EMC, and gradually increases to nearly 1 until 4.15 V, representing the desolvation is at high SOC. After 4.15 V, the ratio of EC/EC-Li^+ remains almost unchanged. In the meantime,

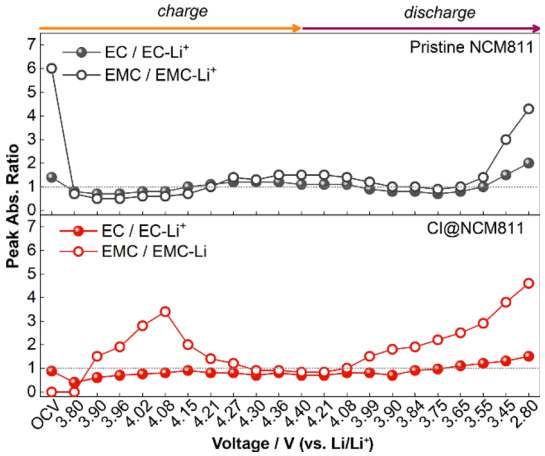

Fig. 6 Li^+ solvation behavior comparison of (a) pristine NCM811 and (b) CI@NCM811 represented by a ratio of EC/EC-Li^+ and EMC/EMC-Li^+. EC is present at 1806 cm^{-1}, EC-Li^+ at 1773 cm^{-1}, EMC at 1747 cm^{-1}, and EMC-Li^+ at 1717 cm^{-1}.

Li^+ presents its desolvation with EMC by increasing the ratio (>1) until 4.4 V, indicating that the electrostatic force between EMC and Li^+ was not as strong as that between EC and Li^+ at high SOC. The desolvated EMC (free single molecule) may easily deprotonate at high SOC on the cathode surface, leading to a thicker CEI formation and possible gas evolution.[37] In the case of bare NCM811, Li^+ solvation was controlled by EC and EMC from OCV to 4.15 V, as well as EC alone from 4.15 to 4.4 V. Moreover, upon discharging, the solvation of EMC-Li^+ recovers below 3.99 V, while EC–Li^+ presents small changes during the entire lithiation process, as shown in Fig. 6a.

For CI@NCM811, as previously shown in Fig. 4c, the presence of EMC-Li^+ (1717 cm^{-1}) was undetected at OCV and 3.8 V. This is probably because the intensity of EMC-Li^+ was too low to be detected by *operando* IR. Therefore, in this study, the ratio comparison of EMC/EMC-Li^+ started after 3.9 V. Fig. 6b shows that the solvation of EMC-Li^+ was lower in almost the entire SOC range (ratio >1), particularly after 3.9 V to 4.08 V upon charging, indicating a repulsion of the EMC. The repulsion of the EMC occurred due to the presence of CI, which serves as a bridge function between the electrolyte and cathode surface. The bridge function from CI contains C=O and –OH groups to decrease Li solvation toward EMC, and repulsed the EMC from deprotonation, resulting in less de-H EMC products as confirmed by Fig. 5. In the case of CI@NCM811, the solvation of EC-Li^+ was strong (ratio <1), indicating that Li^+ solvation was solely controlled by EC.

Scheme 1 summarizes the reaction mechanism of EC and EMC on the Ni-rich cathode, which is dominated by the deprotonation with oxide. Conversely, the CI effectively reduced the deprotonation of EC and EMC, which causes less CEI to be formed and further improves the battery performance.

Electrochemical properties

The electrochemical properties of CI on NCM811 were first evaluated by cyclic voltammetry. Fig. 7a and b shows three redox couples in the scan range of 2.8–4.6 V. The first couple in the range of 3.6–3.8 V can be assigned to the first hexagonal (H1) to monoclinic (M) phase transition, followed by monoclinic (M) to the second hexagonal (H2) from 3.95–4.05 V, then the second hexagonal (H2) to the third hexagonal (H3) at 4.15–4.25 V.[39–42] The first redox couple had a voltage difference of 290 mV at the first cycle, followed by 90 mV at the second cycle for pristine NCM811, as shown in Fig. 7a and b. In the case of CI@NCM811, the voltage differences for the first cycle and second cycle were 320 mV and 50 mV, respectively (Fig. 7a and b). This result showed that the reversibility behavior and reaction kinetics of CI@NCM811 at the first cycle is lower than that for pristine NCM811. Fortunately, this phenomenon is completely eliminated in the following scans: the second scan shows a voltage

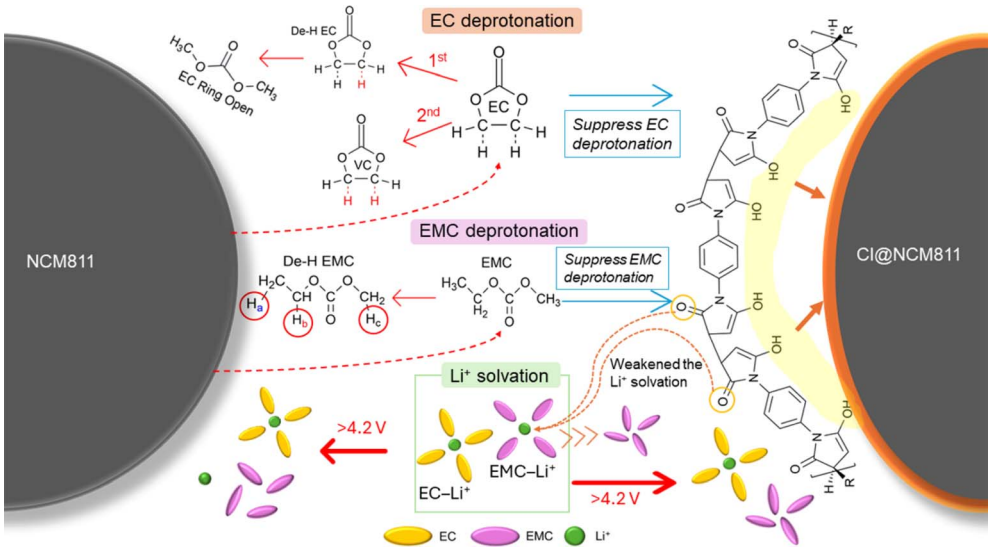

Scheme 1 Proposed reaction mechanisms of EC and EMC on (left panel) NCM811 and (right panel) the bridge function of the CI layer on NCM811.

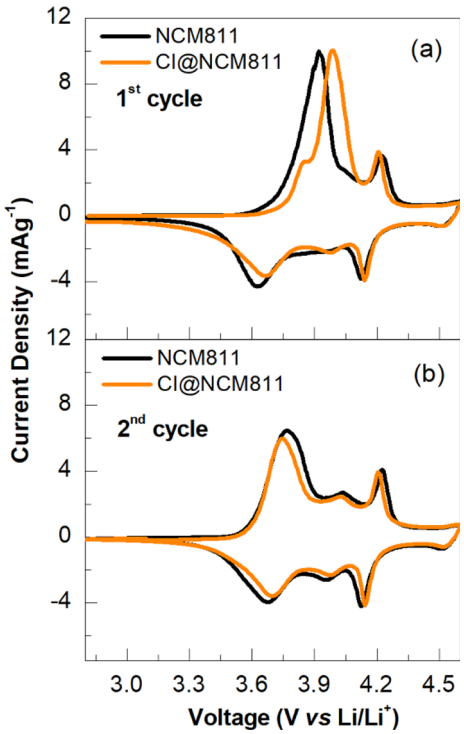

Fig. 7 Cyclic voltammetry curves of pristine NCM811 and CI@NCM811 at (a) the 1st cycle and (b) 2nd cycle with a scan rate of 0.1 mV s^{-1} in the range of 2.8–4.6 V.

difference of only ~50 mV. According to the Nicholson–Shain current function, a voltage difference of 57–60 mV in a redox couple indicated the good reversibility of the CI layer on NCM811.[41]

The low reversibility at the first cycle of CI@NCM811 can be due to the presence of a small shoulder (~3.85 V) near the main anodic reaction (3.98 V, as shown in Fig. 7a). The previous studies stated that the H1-to-M phase transition in the first scan is found at 3.90 V for the Ni^{2+}-to-Ni^{3+} reaction.[43] The bond length of Ni–O is shortened as the Ni ion valence increases during the phase transition from H1 to M, thereby increasing the negativity of the O atom.[18,44] The highly negative O atom, which is supposed to induce the carbonate solvent deprotonation, tends to dissociate the proton of CI instead and forms an activation reaction in the H1-to-M phase transition. The activation reaction of CI was confirmed by the *operando* FTIR result in Fig. 3. The deprotonation and decomposition products of EC (de-H EC, VC, C–O–C stretching and O–C=O bending) from CI@NCM811 were detected at 3.9 V, which is delayed compared to pristine NCM811 (at 3.8 V). In addition, the activation potential of CI was found to be the same as the voltage where EMC repulsion taking place (as shown in Fig. 6b). This result implies that by decreasing the EMC-Li^+ solvation, the bridge function of CI slightly reduces the reversibility of the lithium ion on the first cycle.

In fact, it is found that the CI effects can be verified by understanding the changes in the Ni ion valence and the bond length of Ni–O/Ni–Ni upon the first delithiation of two cathode materials. Fig. S6 and S7† show the *in situ* XANES and EXAFS spectra of the Ni K edge to understand the changes in the Ni ion valence and the bond length of Ni–O/Ni–Ni in the first delithiation. Both pristine NCM811 and CI@NCM811 in Fig. S6a–d† show the increasing of Ni ion valence to higher state during the initial delithiation process. The shifting of the edge jump is summarized in Fig. S6e,† where the CI@NCM811 exhibits a higher valence state than the pristine NCM811 upon charging at 3.9 V. It is comparable with the CV result in that an activation of CI @NCM811 occurs in this voltage range, and thereby causes a change in the bond length of Ni–O or Ni–Ni in the potential range of H1-to-M phase transition. Furthermore, this higher nickel valence state of CI@NCM811 at 3.9 V indicates that the CI coverage blocked the transition metal reduction, which induces the deprotonation of EC to VC.[10]

In situ EXAFS revealed the changing behavior on the Ni–O or Ni–Ni bonds in terms of the delithiation reaction. Fig. S7† reveals that the Ni–O bond (the first shell) of pristine NCM811 exhibits a longer length (2.11 Å) than that of the CI@NCM811 (1.98 Å) at the OCV, indicating a strong correlation between the oxygen atom and the CI. This shortened length on the Ni–O bond of CI@NCM811 is beneficial to prevent the TM reduction, which can cause deprotonation of EC, as described above. Therefore, in agreement with the *operando* IR results, the CI@NCM811 contained less deprotonation of carbonates solvents, as shown in Fig. 3.

With the increase in the voltage, the Ni–O bond length of bare NCM811 is shortened from OCV to 3.9 V, and is followed by a shift of the Ni–Ni shell to a lower bond length from 3.9 to 4.5 V (Fig. S7†). From this viewpoint, the deprotonation of the carbonates is suggested from the Ni–O bond first and further induces oxygen release, thereby changing the Ni–Ni bond length at high SOC. On the contrary, CI@NCM811 shows that the Ni–O bond is not significantly different as the voltage increases.

The cycle performance on CI@NCM811 was operated in a half-cells test to investigate how the deprotonation of carbonates is prevented, and a good ionic transfer is delivered in terms of its cis structure formulation. Fig. S8† shows the initial charge–discharge profile of the pristine NCM811 and CI@NCM811 electrodes conducted at 0.1C current rate in the potential range of 2.8–4.3 V (*vs.* Li/Li^+). The initial discharge capacities (Coulombic efficiency) of the pristine NCM811 and CI@NCM811 were 205.11 mA h g^{-1} (87.3%) and 205.28 mA h g^{-1} (86.9%), respectively. This result confirms that CI activation induces a slight loss of coulombic efficiency in the first cycle, which is consistent with the CV result (Fig. 7a). Pristine NCM811 retained 21.5% of its initial capacity at the 250th cycle (Fig. 8a). In contrast, at the 250th cycle, CI@NCM811 maintained 79.2% of its initial capacity. By the CI coverage, the carbonate decomposition on the cathode surface could be effectively prevented, *i.e.*, there would be a decrease in the deprotonation. Moreover, the surface morphology by SEM analysis after 250 cycles revealed that several small dots were spread on the pristine NCM811 surface, which can be attributed to the CEI (Fig. S9a and b†). Meanwhile, Fig. S9c and d† displays a clean surface on CI@NCM811, indicating that the CEI is

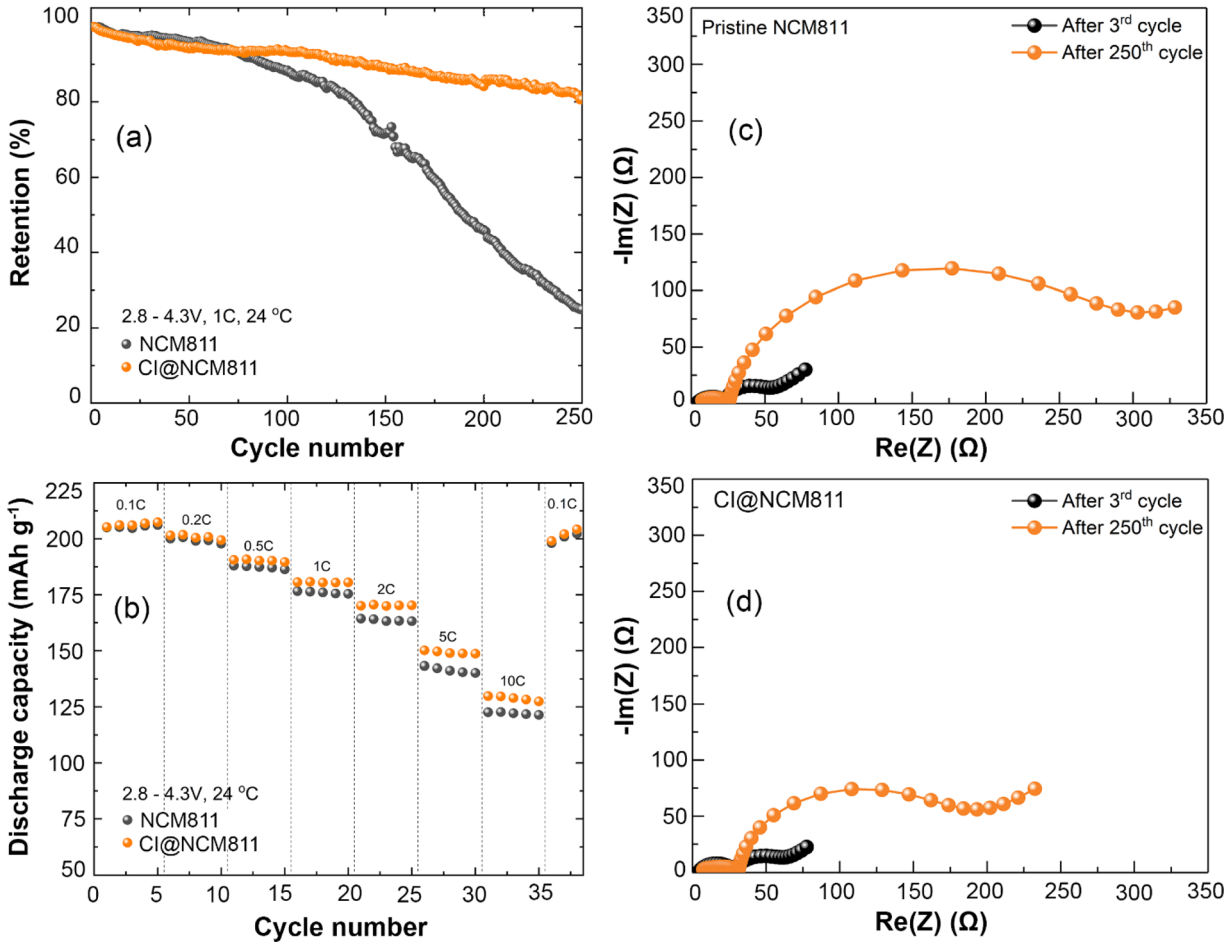

Fig. 8 (a) Cycle retention at room temperature and (b) rate capability of pristine NCM811 and CI@NCM811 in the half-cell test. The Nyquist plots of (c) pristine NCM811 and (d) CI@NCM811.

significantly minimized by the inhibition of carbonate deprotonation. Nevertheless, the coverage of CI on NCM811 slightly improved the half-cell rate capability at above 1C (Fig. 8b). The lithium diffusion coefficient (D_{Li^+}) was also calculated from the Warburg tail of the EIS spectra at the charge potential of ~3.9 V, as described and presented in ESI, Fig. S10.† The calculated Li^+ diffusion coefficient in a prolonged cycle is 3.82×10^{-8} cm^2 s^{-1} and 4.48×10^{-8} cm^2 s^{-1} for pristine NCM811 and CI@NCM811, respectively. Besides the C=O functional group that attracts Li^+, the increasing D_{Li^+} is likely also contributed from the phenyl group which resembles a ring-like structure that keeps the CI pore size adequately large for the Li^+ migration.[45]

The impedance analysis concerning the first and 250th cycles is shown in Fig. 8c and d. The two semi-circles of the two electrodes, represent three specific features regarding the equivalent circuit model (Fig. S11†), electrolyte resistance (R_e), CEI resistance (R_{cei}), and charge transfer resistance (R_{ct}), respectively.[46,47] The pristine NCM811 exhibited R_e, R_{cei}, and R_{ct} values of 3.8, 21.5, and 48.1 Ω after the initial cycle, respectively. In comparison, CI@NCM811 exhibited R_e, R_{cei}, and R_{ct} values of 3.9, 28.2, and 59.8 Ω after the initial cycle, respectively. The CI coverage affected the impedance on both cathode surface (R_{cei}) and the electrochemical reaction (R_{ct}). Similar to the CV shown in Fig. 7a, an interaction of CI occurs in the H1-to-M phase transformation, making the electron transfer initially slow. After the 250th cycle, the R_{ct} value of pristine NCM811 was 279.9 Ω, and increased almost 6 times higher compared to its formation condition. In contrast, the R_{ct} value of CI@NCM811 (173.8 Ω) only increased 4 times from its formation cycle. This impedance analysis is consistent with the above discussions on the bridge function of CI protecting the electrode–electrolyte side reactions. Thus, in a prolonged cycle, CI@NCM811 has a slower growth of impedance, which provides a significantly better cycle stability than pristine NCM811.

To further investigate the CI effects of the dynamic performance characteristics of a full-cell, a Hybrid Pulse Power Characterization (HPPC) test was used for evaluation. This test determined the cell power capability over the useable voltage range of the cell. It is a test profile that incorporates both discharging and regeneration (recharging) pulses at various DOD. A discharge pulse is a relatively short load drawn on the battery, and a regeneration pulse is a relatively short charge to the battery. This profile mimics the discharge and charge that can occur on hybrid EVs during acceleration and regenerative

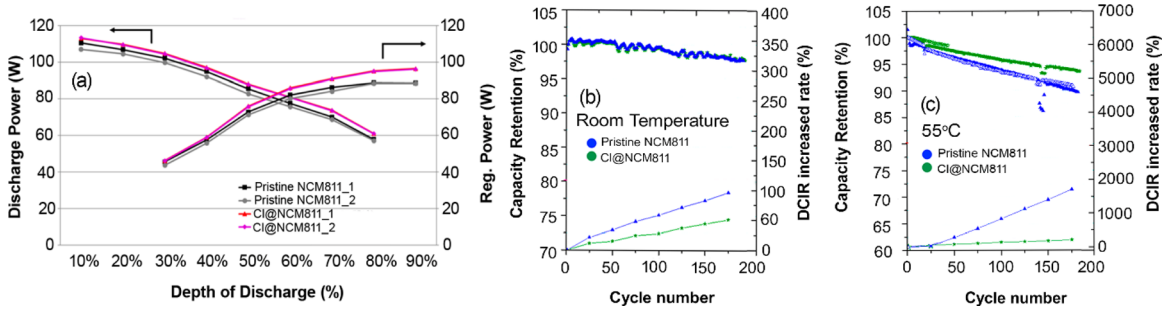

Fig. 9 Full cell (>3 A h) test on (a) HPPC analysis, cycling performances at (b) room temperature and (c) 55 °C; the corresponding DCIR of pristine NCM811 and CI@NCM811 is included.

breaking.[36,37] Fig. 9a shows the HPPC results in terms of the two full cells. For the pristine NCM811, the power provided at each 10% DOD of the discharging reaction was lower than that for CI@NCM811. The power delivered by the pristine NCM811 at 10% DOD was approximately in the range of 105–108 W compared with that delivered by CI@NCM811 (113.6 W). The capacity of this full cell was set to 3 A h with an average working voltage of 3.7 V. Thus, 100 W represents almost 9C in a fully operational range. In the case of the regeneration power (recharging) analysis, at 90% DOD, CI@NCM811 provided a fast-recharging power (96.5 W) until a DOD of 40% (59.6 W), which is also higher than that of the pristine NCM811. These results demonstrate that a deprotonation of the carbonate solvents on the Ni-rich cathode surface is necessary, which can significantly improve the battery rate capability through CI coverage, typically in the low-to-medium SOC range. With the CI coverage, this full cell charges from 10% to 70% SOC, which takes only 6.25 min in terms of the HPPC analysis.

Fig. 9b and c shows the full cell (>3A h) tested at 1C/1C at room temperature and at 55 °C for evaluating the aging effect on its direct circuit internal resistance (DCIR). Evidently, a high temperature triggers a faster fading behavior of the pristine NCM811, which is due to the increment in the DCIR. At room temperature, the cycle retention between the two full-cells was not shown to be different for 200 cycles, and the DCIR exhibits a significant difference. The pristine NCM811 exhibits a value that is almost twice that of CI@NCM811. This result is consistent with the impedance analysis (Fig. 8c and d). In the experiment conducted at a temperature of 55 °C, the aging effect dramatically exhibited a rapid fading behavior on cycle retention, as well as the DCIR, with the pristine NCM811 cell showing a significantly worse fading behavior than CI@NCM811. This result clearly demonstrates the effect of the presence of CEI on the Ni-rich cathode at high temperature. Thus, the CI containing the cis structure effectively contributed as a bridge function on the cathode surface.

Conclusions

In this work, the deprotonation mechanism of carbonates was clarified by *operando* FTIR. EC proceeded *via* two pathways, namely VC formation and ring opening, in the very early reaction step (3.8 V). The EMC was deprotonated mainly at its *b* site based on the asymmetrical structure. However, we discovered that EMC deprotonated at the *a* and *c* sites as well. A new material was synthesized for surface coverage on the Ni-rich cathode: a CI oligomer. With the cis structure formulation of the CI, the oxygen atom on the NCM811 surface could deprotonate the CI rather than the carbonates, termed as a bridge function. In addition, the C=O bond side of the CI was used to attract Li^+ to enhance the ionic diffusivity during cycling. EMC was not deprotonated on CI@NCM811, which significantly eliminated the CEI formation on the cathode. Moreover, the CI adjusted the solvation characteristics of the carbonate solvent in electrolytes. Thus, it could indicate a controllable CEI formation on NCM811.

Data availability

Data will be made available on request. The data supporting this article have been included as part of the ESI.†

Author contributions

Laurien Merinda: writing – original draft, methodology, investigation, validation. Fu-Ming Wang: conceptualization, investigation, project administration, supervision, writing – review & editing, resources. Nae-Lih Wu: investigation, funding acquisition, supervision, validation, resources. Rio Akbar Yuwono: validation, formal analysis, methodology, writing – review & editing. Chusnul Khotimah: visualization, formal analysis, validation. Ulya Qonita: visualization. Wei-Hsiang Huang: data curation. Lester Pei-Wan Tiong: data curation. Ching-Kai Chang: investigation. Ping-Hsuan Hsu: data curation. Chih-Wen Pao: resources. Jeng-Lung Chen: resources. Chi-Liang Chen: resources. Ting-Shan Chan: resources.

Conflicts of interest

The authors declare that they have no known competing financial interests or personal relationships that could have appeared to influence the work reported in this paper.

Acknowledgements

F. M. Wang is grateful for the financial support from the National Science and Technology Council (NSTC) and the Ministry of Education (MOE, "Sustainable Electrochemical Energy Development Center" (SEED)) project of Taiwan, R.O.C., under grant numbers 110-2923-E-007-005, 111-2622-E-011-013-, 111-3116-F-011-005-, 112-2923-E-007-005, 112-2622-E-011-026, and 112-2221-E-011-013-MY3. N. L. Wu thanks the financial support of the "Advanced Research Center for Green Materials Science and Technology" (Ministry of Education (TW), project number: 112L9006) and of the National Science and Technology Council (TW) under contract number of NSTC-110-2221-E-002-015-MY3 and 112-2923-E-011-005.

References

1 W. Li, E. M. Erickson and A. Manthiram, *Nat. Energy*, 2020, **5**, 26–34.
2 IEA, *World Energy Outlook 2023*, **https://www.iea.org/reports/world-energy-outlook-2023**, (accessed July 25, 2024).
3 S.-M. Bak, E. Hu, Y. Zhou, X. Yu, S. D. Senanayake, S.-J. Cho, K.-B. Kim, K. Y. Chung, X.-Q. Yang and K.-W. Nam, *ACS Appl. Mater. Interfaces*, 2014, **6**, 22594–22601.
4 X. Zeng, C. Zhan, J. Lu and K. Amine, *Chem*, 2018, **4**, 690–704.
5 H.-R. Kim, S.-G. Woo, J.-H. Kim, W. Cho and Y.-J. Kim, *J. Electroanal. Chem.*, 2016, **782**, 168–173.
6 H.-J. Noh, S. Youn, C. S. Yoon and Y.-K. Sun, *J. Power Sources*, 2013, **233**, 121–130.
7 W. Li, H. Y. Asl, Q. Xie and A. Manthiram, *J. Am. Chem. Soc.*, 2019, **141**, 5097–5101.
8 Y. Zhang, Y. Katayama, R. Tatara, L. Giordano, Y. Yu, D. Fraggedakis, J. G. Sun, F. Maglia, R. Jung, M. Z. Bazant and Y. Shao-Horn, *Energy Environ. Sci.*, 2020, **13**, 183–199.
9 D. Streich, C. Erk, A. Guéguen, P. Müller, F.-F. Chesneau and E. J. Berg, *J. Phys. Chem. C*, 2017, **121**, 13481–13486.
10 B. L. D. Rinkel, J. P. Vivek, N. Garcia-Araez and C. P. Grey, *Energy Environ. Sci.*, 2022, **15**, 3416–3438.
11 D. J. Miller, C. Proff, J. G. Wen, D. P. Abraham and J. Bareño, *Adv. Energy Mater.*, 2013, **3**, 1098–1103.
12 S. Watanabe, M. Kinoshita, T. Hosokawa, K. Morigaki and K. Nakura, *J. Power Sources*, 2014, **258**, 210–217.
13 R. A. Yuwono, C. Khotimah, F.-M. Wang, N.-L. Wu, A. C. Imawan, R. Foeng, P.-C. Huang, G.-Y. Liu, S.-C. Haw and H.-S. Sheu, *J. Energy Storage*, 2024, **92**, 112184.
14 R. Jung, M. Metzger, F. Maglia, C. Stinner and H. A. Gasteiger, *J. Electrochem. Soc.*, 2017, **164**, A1361–A1377.
15 L. A. Kaufman and B. D. McCloskey, *Chem. Mater.*, 2021, **33**, 4170–4176.
16 A. T. S. Freiberg, J. Sicklinger, S. Solchenbach and H. A. Gasteiger, *Electrochim. Acta*, 2020, **346**, 136271.
17 R. Jung, M. Metzger, F. Maglia, C. Stinner and H. A. Gasteiger, *J. Phys. Chem. Lett.*, 2017, **8**, 4820–4825.
18 Y. Yu, P. Karayaylali, Y. Katayama, L. Giordano, M. Gauthier, F. Maglia, R. Jung, I. Lund and Y. Shao-Horn, *J. Phys. Chem. C*, 2018, **122**, 27368–27382.
19 Y. Zhang, Y. Song and J. Liu, *ACS Appl. Mater. Interfaces*, 2023, **15**, 19075–19084.
20 L. Dou, A. Tang, W. Lin, X. Dong, L. Lu, C. Shang, Z. Zhang, Z. Huang, K. Aifantis, P. Hu and D. Xiao, *Electrochim. Acta*, 2022, **425**, 140745.
21 S. N. Lauro, J. N. Burrow and C. B. Mullins, *eScience*, 2023, **3**, 100152.
22 F.-M. Wang, T. Alemu, N.-H. Yeh, X.-C. Wang, Y.-W. Lin, C.-C. Hsu, Y.-J. Chang, C.-H. Liu, C.-I. Chuang, L.-H. Hsiao, J.-M. Chen, S.-C. Haw, W.-L. Chen, Q.-T. Pham and C.-H. Su, *ACS Appl. Mater. Interfaces*, 2019, **11**, 39827–39840.
23 N.-H. Yeh, F.-M. Wang, C. Khotimah, X.-C. Wang, Y.-W. Lin, S.-C. Chang, C.-C. Hsu, Y.-J. Chang, L. Tiong, C.-H. Liu, Y.-R. Lu, Y.-F. Liao, C.-K. Chang, S.-C. Haw, C.-W. Pao, J.-L. Chen, C.-L. Chen, J.-F. Lee, T.-S. Chan, H.-S. Sheu, J.-M. Chen, A. Ramar and C.-H. Su, *ACS Appl. Mater. Interfaces*, 2021, **13**, 7355–7369.
24 Y.-H. Li, M.-L. Lee, F.-M. Wang, C.-R. Yang, P. P. J. Chu, S.-L. Yau and J.-P. Pan, *Appl. Surf. Sci.*, 2012, **261**, 306–311.
25 Y. Yu, Y. Zhang, L. Giordano, Y. G. Zhu, F. Maglia, R. Jung, F. S. Gittleson and Y. Shao-Horn, *J. Electrochem. Soc.*, 2021, **168**, 060538.
26 L. Giordano, P. Karayaylali, Y. Yu, Y. Katayama, F. Maglia, S. Lux and Y. Shao-Horn, *J. Phys. Chem. Lett.*, 2017, **8**, 3881–3887.
27 M. M. Amaral, C. G. Real, V. Y. Yukuhiro, G. Doubek, P. S. Fernandez, G. Singh and H. Zanin, *J. Energy Chem.*, 2023, **81**, 472–491.
28 I. Hasa, A. M. Haregewoin, L. Zhang, W.-Y. Tsai, J. Guo, G. M. Veith, P. N. Ross and R. Kostecki, *ACS Appl. Mater. Interfaces*, 2020, **12**, 40879–40890.
29 M. Matsui, K. Dokko and K. Kanamura, *J. Electrochem. Soc.*, 2010, **157**, A121.
30 M. Tesemma, F.-M. Wang, A. M. Haregewoin, N. L. Hamidah, P. Muhammad Hendra, S. D. Lin, C.-S. Chern, Q.-T. Pham and C.-H. Su, *ACS Sustainable Chem. Eng.*, 2019, **7**, 6640–6653.
31 J. Wandt, A. T. S. Freiberg, A. Ogrodnik and H. A. Gasteiger, *Mater. Today*, 2018, **21**, 825–833.
32 B. L. D. Rinkel, D. S. Hall, I. Temprano and C. P. Grey, *J. Am. Chem. Soc.*, 2020, **142**, 15058–15074.
33 Q. Chen, Y. Pei, H. Chen, Y. Song, L. Zhen, C.-Y. Xu, P. Xiao and G. Henkelman, *Nat. Commun.*, 2020, **11**, 3411.
34 J. Ma, G. Sun, D. Sun, F. Yu, M. Hu and T. Lu, *Constr. Build. Mater.*, 2021, **278**, 122386.
35 C. John, *Interpretation of Infrared Spectra, a Practical Approach*, John Wiley & Sons Ltd, Chichester, 2000.
36 C.-C. Su, M. He, R. Amine, Z. Chen, Z. Yu, T. Rojas, L. Cheng, A. T. Ngo and K. Amine, *Nano Energy*, 2021, **83**, 105843.
37 W. M. Dose, I. Temprano, J. P. Allen, E. Björklund, C. A. O'Keefe, W. Li, B. L. Mehdi, R. S. Weatherup, M. F. L. De Volder and C. P. Grey, *ACS Appl. Mater. Interfaces*, 2022, **14**, 13206–13222.
38 M. Gauthier, P. Karayaylali, L. Giordano, S. Feng, S. F. Lux, F. Maglia, P. Lamp and Y. Shao-Horn, *J. Electrochem. Soc.*, 2018, **165**, A1377–A1387.

39 M. Jiang, D. L. Danilov, R. Eichel and P. H. L. Notten, *Adv. Energy Mater.*, 2021, **11**, 2103005.
40 L. De Biasi, B. Schwarz, T. Brezesinski, P. Hartmann, J. Janek and H. Ehrenberg, *Adv. Mater.*, 2019, **31**, 1900985.
41 F. Wu, N. Liu, L. Chen, Y. Su, G. Tan, L. Bao, Q. Zhang, Y. Lu, J. Wang, S. Chen and J. Tan, *Nano Energy*, 2019, **59**, 50–57.
42 R. A. Yuwono, F.-M. Wang, N.-L. Wu, Y.-C. Chen, H. Chen, J.-M. Chen, S.-C. Haw, J.-F. Lee, R.-K. Xie, H.-S. Sheu, P.-Y. Chang, C. Khotimah, L. Merinda and R. Hsing, *Chem. Eng. J.*, 2023, **456**, 141065.
43 B. H. Vassos and G. W. Ewing, *Electroanalytical Chemistry*, Wiley, New York, 1983.
44 C. Xu, P. J. Reeves, Q. Jacquet and C. P. Grey, *Adv. Energy Mater.*, 2021, **11**, 2003404.
45 Y.-C. Wen, Y.-C. Sue, S.-Y. Yang, J.-P. Pan, T.-H. Wang and H.-W. Jia, *RSC Adv.*, 2017, **7**, 651–661.
46 F.-M. Wang, E. B. Chemere, W.-C. Chien, C.-L. Chen, C.-C. Hsu, N.-H. Yeh, Y.-S. Wu, C. Khotimah, K. W. Guji and L. Merinda, *ACS Appl. Mater. Interfaces*, 2021, **13**, 46703–46716.
47 F.-M. Wang, D.-T. Shieh, J.-H. Cheng and C.-R. Yang, *Solid State Ionics*, 2010, **180**, 1660–1666.